

Non-classical mechanical states guided in a phononic waveguide

Amirparsa Zivari, Robert Stockill, Niccolò Fiaschi, and Simon Gröblacher*

*Kavli Institute of Nanoscience, Department of Quantum Nanoscience,
Delft University of Technology, 2628CJ Delft, The Netherlands*

Quantum optics – the creation, manipulation and detection of non-classical states of light – is a fundamental cornerstone of modern physics, with many applications in basic and applied science. Achieving the same level of control over phonons, the quanta of vibrations, could have a similar impact, in particular on the fields of quantum sensing and quantum information processing. Here we demonstrate the first step towards this level of control and realize a single-mode waveguide for individual phonons in a suspended silicon micro-structure. We use a cavity-waveguide architecture, where the cavity is used as a source and detector for the mechanical excitations, while the waveguide has a free standing end in order to reflect the phonons. This enables us to observe multiple round-trips of the phonons between the source and the reflector. The long mechanical lifetime of almost 100 μs demonstrates the possibility of nearly lossless transmission of single phonons over, in principle, tens of centimeters. Our experiment represents the first demonstration of full on-chip control over traveling single phonons strongly confined in the directions transverse to the propagation axis and paves the way to a time-encoded multimode quantum memory at telecom wavelength and advanced quantum acoustics experiments.

Creating and detecting quantum states of mechanical motion open up new possibilities for quantum information processing, quantum sensing and probing the foundations of quantum physics [1]. In particular within the field of quantum optomechanics many remarkable milestones have been reached over the past years: from showing the ability to realize the quantum ground state of a mechanical oscillator and single phonon control [2], unambiguous demonstration of the quantum nature of phonons through the creation of entangled states [3–5] and a Bell test [6], to realizing a long coherence-time quantum memory [7]. Furthermore, the field has shown the potential to enable crucial applications in connecting quantum computers, and transfer information between them [8–11]. While these applications usually rely on highly confined phononic states (with a typical mode volume on the order of the wavelength), the use of traveling phonons promises the ability to create on-chip architectures for classical and quantum information [12], with the potential to add completely new capabilities compared to their optical counterparts. The exciting prospects in this new field of quantum acoustics are enabled by the orders of magnitude slower propagation speed compared to photons, the inherently low loss, their extremely low energy and the small mode volume compared to GHz-frequency photons. These features make phonons ideally suited for direct manipulation on a chip with wavelength sized components, while the ability to realize significant time-delays in a short distance makes this type of system an ideal platform for on-chip operations [13]. Furthermore, phonons have also demonstrated their unique capability to efficiently couple and even mediate the interaction between various quantum systems [14], such as

superconducting qubits [15], defect centers in solids [16], and quantum dots [17, 18]. Using mechanical excitations as low-loss carriers of quantum information will allow for the construction of two-dimensional architectures and large-scale phononic quantum networks [19].

While the creation of non-classical mechanical states have been demonstrated in multiple physical systems [20], only a very limited number of experiments have been able to realize propagating modes in the quantum regime, all based on surface acoustic waves [15, 21, 22]. This approach comes with its own limitations and challenges, such as relatively short lifetimes, losses due to beam steering and diffraction, typically only bi-directional emission and no full confinement of the mode except in resonators. In the classical domain on the other hand, several proof-of-concept experiments have realized the creation, transport and detection of mechanical states at cryogenic temperatures [23] over millimeter ranges, as well as at room temperature and atmospheric pressure [24]. The possibility of guiding a mechanical quantum state in a waveguide that confines the excitation in all directions transverse to its propagation, similar to optical fibers and waveguides, remains an open challenge.

Here we demonstrate a single-mode phononic waveguide directly coupled to an on-chip source and detector for non-classical mechanical states. We verify the non-classicality of the launched mechanical states by measuring their quantum correlations with an optical read-out field. In particular, we use the optomechanical interaction to herald the creation of a single phonon, which then leaks into the phononic waveguide. Since the waveguide has a free standing end that acts as a mirror for the phonons, the excitations bounce back and forth with a certain characteristic time that is determined by the group velocity and the length of the waveguide. Moreover, we observe non-classical correlations between time-

* s.groeblicher@tudelft.nl

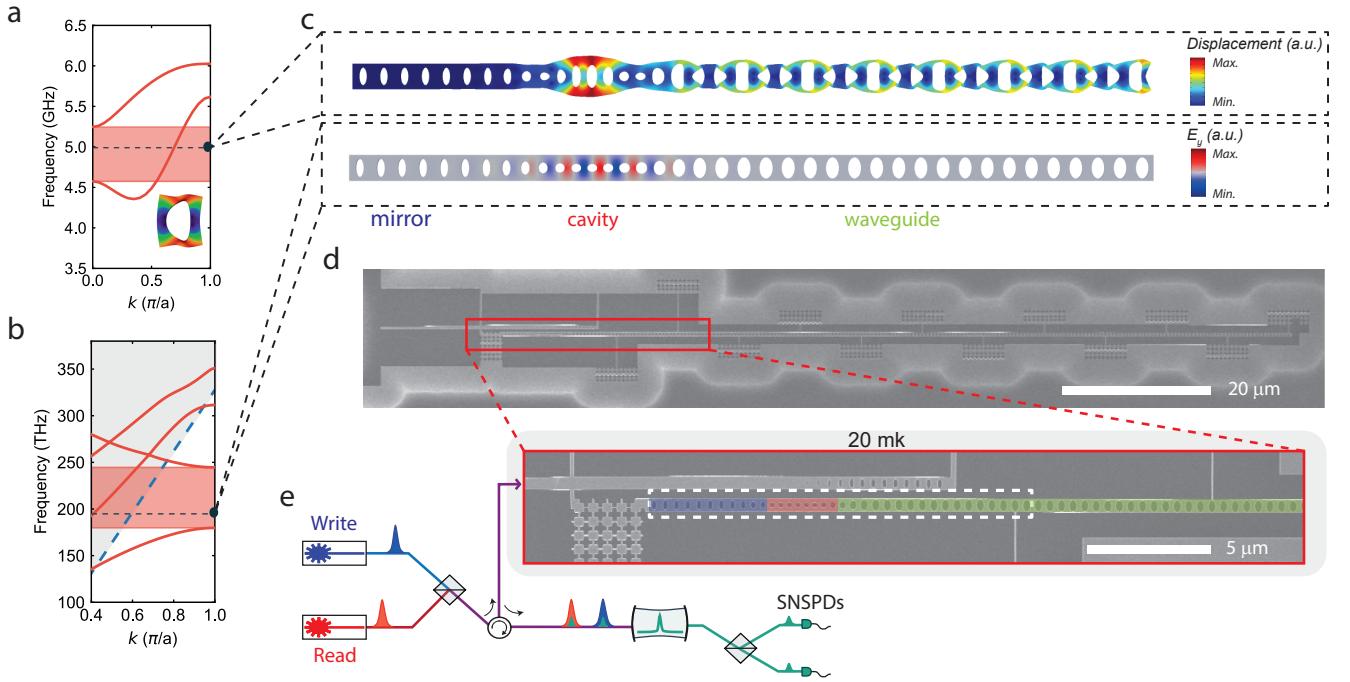


FIG. 1. a) Band diagram for the modes with symmetric displacement field with respect to the propagation direction along the waveguide. These modes are expected to couple efficiently to the resonant optomechanical cavity mode. The highlighted region (red) shows a single mode waveguide with linear dispersion. The dashed line represent the frequency of the modes of the optomechanical structure. Inset: mode shape of the unit cell from this simulation for the band of interested. b) Band diagram for the optical TE mode of the phononic waveguide, exhibiting a band gap at telecom wavelengths, allowing for a confined optical mode inside the optomechanical resonator. The dashed blue line is the light cone, with the non guided modes in the gray shaded area. c) Mechanical (top) and optical (bottom) eigenfrequency simulation of the full cavity and waveguide structure. Clearly visible are the resonant breathing mode of the optomechanical crystal (left) and the waveguide mode (right). As the mechanical mode leaks through the waveguide, the optical mode stays confined inside the optomechanical resonator. d) A scanning electron microscope image of the device used in the experiment, showing the full device with mirror, cavity and the $92\ \mu\text{m}$ long waveguide, as well as the optical coupling waveguide (top left). e) Schematic of the setup together with a zoomed-in section of (d) (indicated by the red box). The blue, red and green shaded regions show mirror, cavity and waveguide, respectively. The white dashed rectangle is the area of the simulation in (c). See the text and SI for a more details.

bin encoded phonons [25], by creating and detecting a phonon either earlier or later. The long lifetime of the device will also allow the creation of an on-chip network for quantum acoustic experiments. With the on-chip source, detector and waveguide presented in this work, only a phononic beam splitter and phase modulator need to be developed in order to obtain full coherent control over phonons on a chip.

We design our phononic crystal waveguide in thin-film silicon, which is single-mode for the symmetric breathing mode of the structure, in the frequency range of interest (at around 5 GHz with a single mode range of 750 MHz) and has an approximately linear dispersion, in order to maintain the spatial mode shape of the traveling phonons. This waveguide is connected to an optomechanical resonator acting as the single-phonon source and detector. For the waveguide design, only the symmetric breathing mode is considered, in order to enable a good mode overlap with the mode of the optomechanical cav-

ity, as these resonant modes have large optomechanical coupling, and can easily be created and detected optically. At the same time, in order to realize a high-finesse optical cavity, we design our phononic waveguide to act as a mirror for photons, therefore confining the optical field in the optomechanical resonator.

The details of our design are shown in Fig. 1a and 1b, where we plot the band structure with the right mechanical symmetry, as well as the transverse electric (TE) polarized optical mode. An eigenvalue simulation of the full structure, cavity and waveguide, is shown in Fig. 1c. The mechanical mode extends into the waveguide, while the optical mode is strongly confined to the cavity region with a similar mode volume to previous works [4, 26–28]. The different sizes of the holes in the structure create the mirror, defect and waveguide. The hole dimensions and periodicity in the waveguide part are adjusted to tune the group velocity. We design the waveguide to have a small group velocity while still having a linear band inside

the frequency range of interest (see SI for more details). From the simulated group velocity, the time duration of the mechanical packet (set by the optical pulse length of 40 ns), and the time of the mechanical excitation to leak from the cavity to the waveguide, we determine a minimum length of about 40 μm for the waveguide for the excitation to completely leave the cavity before it comes back again, which is why we choose a length of 92 μm .

A picture of the device and sketch of the experimental setup can be found in Figure 1d-e. To excite and detect non-classical phonons we use laser pulses detuned from the optical resonance to address the optomechanical Stokes and anti-Stokes sidebands in order to create (write) the mechanical excitation and to map it onto the optical mode (read), respectively [29]. After being combined on a 50:50 beam splitter (BS), the light is routed via an optical circulator to the device. The reflected light from the device is then filtered using free space Fabry-Pérot cavities and, after another BS, is sent to the superconducting nanowire single photon detectors (SNSPDs). The device itself is cooled to 20 mK in order to initialize the mechanical mode of interest deep in the ground state.

For the initial characterization of the device, we use a tunable continuous-wave (CW) laser to determine the optical resonance in reflection. As shown in Fig. 2a, the fundamental optical resonance has a central wavelength around 1541 nm and a linewidth of $\kappa_t = 1021$ MHz (with extrinsic and intrinsic loss rates of $\kappa_e = 364$ MHz and $\kappa_i = 656$ MHz). We measure the mechanical spectrum using the optomechanical induced transparency (OMIT) technique [30]. The resulting renormalized amplitude of the reflected probe field ($|S_{21}|$) is plotted in Fig 2b, where a series of (almost) equally spaced peaks shows the hybridization of the single mode of the cavity with the series of modes of the free-ended waveguide. We choose the first prominent mechanical resonance (around 4.98 GHz) as the frequency to which we detune the laser with respect to the optical resonance wavelength for addressing the Stokes and anti-Stokes interaction. We further measure the equivalent single photon optomechanical coupling rate from the Stokes scattering probability using a short optical pulse of full width at half maximum (FWHM) ≈ 40 ns, obtaining a collective $g_0/2\pi \approx 460$ kHz (for a detailed explanation see the SI). This is the joint coupling rate of all mechanical eigenmodes within the detection filter bandwidth.

In order to determine the time dynamics of the phononic wave packet, we measure the second order correlation function $g_\tau^{(2)}$ of the light scattered from the cavity with a CW read-out tone detuned to the anti-Stokes sideband. Due to non-negligible optical absorption in silicon, the continuous laser creates a small thermal mechanical population in the device. We obtain the $g_\tau^{(2)}$ between emitted photons from the device, by measuring two photon coincidences on two different SNSPDs and normal-

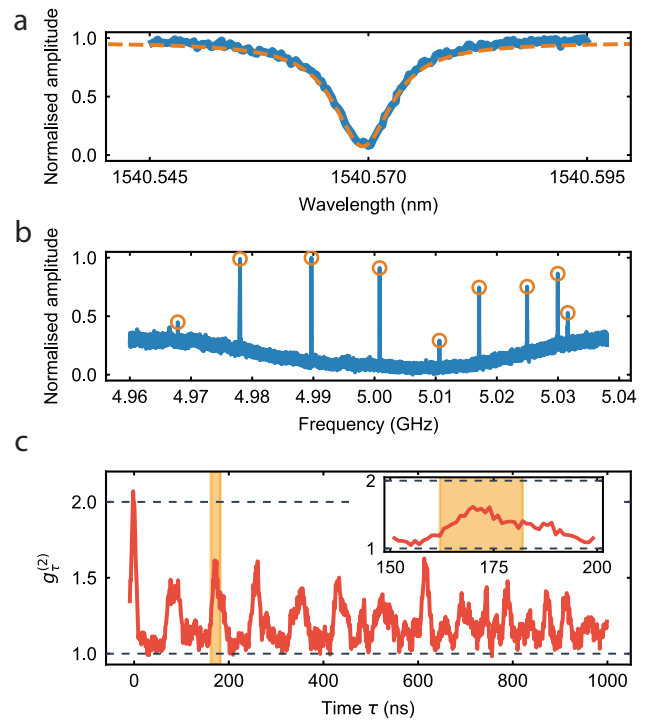


FIG. 2. (a) Characterization of the optical resonance of the device in reflection. (b) Mechanical spectrum measured using the OMIT technique at 20 mK. The series of peaks is given by the hybridization of the cavity mode and the modes of the waveguide (approximately equally spaced). (c) $g_\tau^{(2)}$ of a bouncing thermal state for different delays between two detection events (τ). Note the series of peaks indicating the traveling back and forth of the phonons in the waveguide. The reduced maxima for the bounced peaks is attributed to the non constant FSR. The area highlighted is the chosen bounced peak for the pulsed experiment with single phonon states. Inset: zoom-in around the highlighted area.

izing them to the single photon counts of the SNSPDs. Owing to the optomechanical interaction, this is equivalent to measuring the $g_\tau^{(2)}$ of the mechanical bounced thermal states, for different delays between the SNSPDs clicks τ . The results are plotted in Fig 2c, showing an (almost) equally spaced series of peaks. As expected for a thermal state, at $\tau = 0$, we observe $g_\tau^{(2)} = 2$, which is then modulated as the state leaks into the waveguide. We attribute the reduced maxima for the bounced peaks ($g_\tau^{(2)} \approx 1.5$ instead of 2) to coupling to undesirable asymmetric mechanical modes (which have relatively low optomechanical coupling rate, and thus cannot be detected optically), as well as the non-constant FSR between mechanical modes of the device, which could be caused by the dispersion of the phononic waveguide. The exact effect will require a more detailed theoretical and experimental analysis in the future.

We use three 150-MHz broad filter cavities in series to filter out the strong optical driving pumps, which

also filter the Stokes and anti-Stokes scattered photons within a frequency range of 80 MHz around the setpoint (4.98 GHz). In this way, any signal from the mechanical modes greater than 5.02 GHz is strongly suppressed and hence, only the part of the spectrum with the evenly spaced mechanical modes will contribute considerably to the correlation. These modes build a frequency comb with a free spectral range (FSR) of around 11 MHz, which corresponds to a rephasing time of $1/\text{FSR} = 91$ ns. This is consistent with the bouncing that can be inferred from the measurement, which is around 85 ns.

In order to verify that we can guide a non-classical mechanical state, we employ a scheme in which we herald the creation of a quantum excitation in the optomechanical cavity, which we confirm by swapping out the mechanical excitation to an optical photon after some time and correlating the photon statistics from the two processes [29]. We obtain these correlations by measuring the coincidences between the events on the SNSPDs. We realize this scheme by addressing the Stokes process with a 119 fJ blue-detuned 40 ns laser pulse creating a two-mode squeezed opto-mechanical state with scattering probability of $p_{s,\text{write}} \approx 1.4\%$. Similarly, to readout the mechanical state from the optomechanical cavity, a red-detuned laser pulse with the same energy, duration and scattering probability of $p_{s,\text{read}} \approx 1.4\%$, is sent to the device addressing the anti-Stokes process. These scattering probabilities set the thermal occupation of the mode of interest to $n_{\text{th}} \approx 0.27$ (see SI). The scheme of the pulses can be seen in Fig. 3a and the delay between the red-detuned and blue-detuned pulses is set to approximately the second bouncing time ($\tau \approx 170$ ns). The detection of a single photon in one of the detectors from the blue-detuned pulse heralds the mechanical state of the defect to a single-phonon Fock state [27]. This phonon leaks through the attached phononic waveguide after a short time T_c and bounces back and forth between the defect part and the end of the waveguide. In Figure 2c the highlighted area shows the chosen bounce peak, that has a delay of $\tau \approx 170$ ns, which is much smaller than the measured lifetime $T_1 \approx 78 \mu\text{s}$ for this particular device (on the same chip we also fabricate several structures with much longer lifetimes of up to 5.5 ms, see the SI for more details). We choose to perform the measurement on the second bounce of the phonon and not on the first one (at $\tau \approx 85$ ns) to avoid any overlap between the optical write and read pulses. Another reason for this is to overcome the SNSPDs' dead time of around 100 ns and hence be able to measure coincidences on the same SNSPD as well as from different SNSPDs. We would like to note that the expected cross-correlation between phonons and photons on higher order bounces is expected to be similar or slightly lower as a result of optical absorption and delayed heating [27, 29]. From this measurement, we can also infer the coupling between the cavity and the waveguide from the width of the chosen peak, obtaining a decay

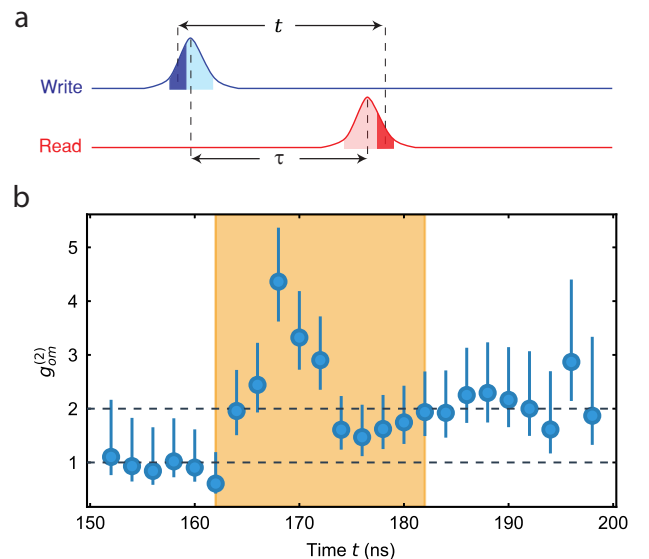


FIG. 3. a) Pulse scheme used for the cross correlation measurement. We fix the time between the pulses to $\tau \approx 170$ ns, as calibrated from the measurement of Fig 2c. In post-processing, we scan a narrow time window of 6 ns with an adjustable delay of t represented by the dark blue and red shaded areas over all of the acquired data (light shaded areas). This approach allows us to calculate the $g_{\text{om}}^{(2)}$ of each point with an adjustable moving window. b) Cross correlation between the optical and the mechanical state for the pulsed experiment $g_{\text{om}}^{(2)}(t)$. The correlation is higher than the classical threshold of 2, with a maxima of $g_{\text{om}}^{(2)} = 4.4^{+1.0}_{-0.7}$, clearly demonstrating the non-classical character of the traveling phonons. For more details on the error calculation see the SI. The highlighted area in the figure has the same position as the one in Fig 2c.

time of $T_c \approx 10$ ns, corresponding to a coupling rate of around $2\pi \times 16$ MHz.

In order to measure the coincidences required to determine the correlations, two 6-ns wide time windows, with a varying delay t between them, are scanned through the whole area of pulses in a post processing step (see Fig. 3a). By summing all the coincidences with each click happening in the same trials ($\Delta n = 0$, for n indicating each round of trial), we gather all the correlated coincidences for each delay. In order to obtain the average uncorrelated coincidences, we perform a similar post processing step, but finding coincidences in different trials ($\Delta n \neq 0$) where the clicks can be assumed to be uncorrelated. Averaging this value over different $\Delta n \neq 0$, gives the average number of uncorrelated coincidences. We use these two values to calculate $g_{\text{om}}^{(2)}(t)$. The time window is chosen to be less than the coupling time between the cavity and the waveguide (T_c) in order to select only the correlated photons that have indeed traveled in the waveguide. The result is shown in Fig. 3b. In order to

gather more statistics, two separate measurements with identical thermal occupation have been used for the data shown here, one with the sequence of red and blue pulses repeated every 200 μs , the other every 300 μs . After merging all the coincidences, a maximum cross-correlation of $g_{\text{om}}^{(2)} = 4.4_{-0.7}^{+1.0}$ is obtained from the bounced phonons at a time of $t = 168$ ns, which is more than 3 standard deviations above the classical threshold of 2, unambiguously showing the non-classical behavior of the guided single phonon state. Furthermore, no non-classical correlations between the photons can be observed at times where the phonon is not spatially located inside the defect (i.e. outside a window of width T_c centered at $t \approx \tau \approx 170$ ns). We suspect the slightly increased correlations at longer times to be a result of the waveguide dispersion. This effect is also clearly visible in the envelope of the second bouncing peak shape in Fig. 2c, with both patterns closely resembling one another.

We further explore the potential of creating a time-bin encoded phononic state by extending our scheme to using two optical excitation (write) and two detection pulses (read), effectively realizing a phononic FIFO quantum memory [31]. The identical blue-detuned optical pulses (FWHM 40 ns) have a scattering probability of $p_{\text{s,write}} \approx 2.7\%$ with $\Delta\tau = 45$ ns delay. The red-detuned detection pulses (FWHM 40 ns) have a scattering probability of $p_{\text{s,read}} \approx 1.5\%$ and with the same time delay. The first blue- and red-detuned pulses are spaced by $\tau = 170$ ns from each other and we repeat this sequence every 800 μs . We then measure the maximum cross correlation in time between all four combinations of write and read pulses, using the same technique for delay-filtering used to extract the data shown in Fig. 3. We choose 40-ns-long non-overlapping time windows to separate "early" write and read pulses from "late" ones, as depicted in Fig. 4a. As shown in Fig. 4b, we can clearly see strong non-classical correlation between the "early-early" and "late-late" combination of excitation and detection pulse, while observing only classical correlations (due to absorption-induced heating) between the other combinations of "early-late" and "late-early".

Our results clearly demonstrate the potential for creating, guiding, and detecting a non-classical mechanical state inside a phononic crystal, using optomechanical techniques. Thanks to the long mechanical lifetime (up to 5.5 ms) and the full lateral confinement, this type of device paves the way towards on-chip quantum acoustic experiments. While some of the motivation for these experiments stems from the similarity to quantum optics, phonons are crucially different, due to the 5 orders of magnitude smaller propagation speed and the ease of coupling them to other quantum systems. The realization of phononic beamsplitters and phase modulators will complete the toolbox required for full control over traveling single phonons and more complex quantum experiments on a chip. Furthermore, the possibility of retrieving the

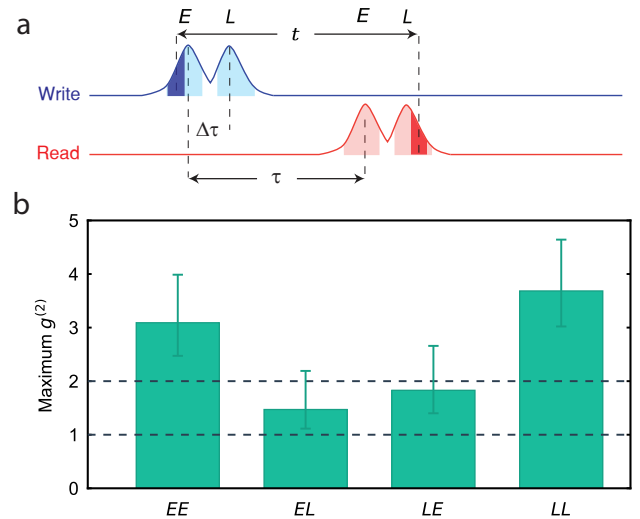


FIG. 4. a) Pulse scheme for the generation of time-bin encoded phonon states with $\Delta\tau = 45$ ns and $\tau = 170$ ns. The area used to gather coincidences is depicted by the light blue (red) shaded area for the write (read) pulses, respectively. In the post-processing step a similar technique as before is used, in order to achieve high timing resolution. An example of 6 ns wide coincidence-filtering windows are sketched by dark blue (red) areas for write (read) pulses for the "early-late" combination. *E* (*L*) stands for early (late). b) As expected, the maximum cross correlations for the various settings clearly shows non-classical correlations for the "early-early" and "late-late" combinations, whereas in the other two we only observe classically correlated phonons.

state after several round-trips and with having time-bin encoded phononic states, together with the full engineerability of the bandstructure, will allow for the creation of time-bin encoded phononic qubits and an optomechanical multimode quantum memory working natively at telecom wavelengths. We also expect guided phonon modes to play a crucial role in the low-energy transmission of quantum information on a chip and for next generation filtering.

We would like to thank Ewold Verhagen and Roel Burgwal for valuable discussions, as well as Moritz Forsch for experimental support. We further acknowledge assistance from the Kavli Nanolab Delft. This work is financially supported by the European Research Council (ERC CoG Q-ECHOS, 101001005), and by the Netherlands Organization for Scientific Research (NWO/OCW), as part of the Frontiers of Nanoscience program, as well as through Vidi (680-47-541/994) and Vrij Programma (680-92-18-04) grants. R.S. also acknowledges funding from the European Union under a Marie Skłodowska-Curie COFUND fellowship.

-
- [1] M. Aspelmeyer, T. J. Kippenberg, and F. Marquardt, Cavity optomechanics, *Rev. Mod. Phys.* **86**, 1391 (2014).
- [2] A. D. O’Connell, M. Hofheinz, M. Ansmann, R. C. Bialczak, M. Lenander, E. Lucero, M. Neeley, D. Sank, H. Wang, M. Weides, J. Wenner, J. M. Martinis, and A. N. Cleland, Quantum ground state and single-phonon control of a mechanical resonator, *Nature* **464**, 697 (2010).
- [3] T. Palomaki, J. Teufel, R. Simmonds, and K. Lehnert, Entangling mechanical motion with microwave fields, *Science* **342**, 710 (2013).
- [4] R. Riedinger, A. Wallucks, I. Marinković, C. Lössnauer, M. Aspelmeyer, S. Hong, and S. Gröblacher, Remote quantum entanglement between two micromechanical oscillators, *Nature* **556**, 473 (2018).
- [5] C. F. Ockeloen-Korppi, E. Damskäg, J.-M. Pirkkalainen, M. Asjad, A. A. Clerk, F. Massel, M. J. Woolley, and M. A. Sillanpää, Stabilized entanglement of massive mechanical oscillators, *Nature* **556**, 478 (2018).
- [6] I. Marinković, A. Wallucks, R. Riedinger, S. Hong, M. Aspelmeyer, and S. Gröblacher, An optomechanical Bell test, *Phys. Rev. Lett.* **121**, 220404 (2018).
- [7] A. Wallucks, I. Marinković, B. Hensen, R. Stockill, and S. Gröblacher, A quantum memory at telecom wavelengths, *Nature Phys.* **16**, 772 (2020).
- [8] R. W. Andrews, R. W. Peterson, T. P. Purdy, K. Cicak, R. W. Simmonds, C. A. Regal, and K. W. Lehnert, Bidirectional and efficient conversion between microwave and optical light, *Nature Phys.* **10**, 321 (2014).
- [9] A. Vainsencher, K. J. Satzinger, G. A. Peairs, and A. N. Cleland, Bi-directional conversion between microwave and optical frequencies in a piezoelectric optomechanical device, *Appl. Phys. Lett.* **109**, 033107 (2016).
- [10] M. Forsch, R. A. Norte, A. Wallucks, I. Marinković, C. Gärtner, R. A. Norte, F. van Otten, A. Fiore, K. Srinivasan, and S. Gröblacher, Microwave-to-optics conversion using a mechanical oscillator in its quantum ground state, *Nature Phys.* **16**, 69 (2020).
- [11] M. Mirhosseini, A. Sipahigil, M. Kalaei, and O. Painter, Superconducting qubit to optical photon transduction, *Nature* **588**, 599 (2020).
- [12] S. J. M. Habraken, K. Stannigel, M. D. Lukin, P. Zoller, and P. Rabl, Continuous mode cooling and phonon routers for phononic quantum networks, *New J. Phys.* **14**, 115004 (2012).
- [13] P. Delsing *et al.*, The 2019 surface acoustic waves roadmap, *J. Phys. D: Appl. Phys.* **52**, 353001 (2019).
- [14] M. J. A. Schuetz, E. M. Kessler, G. Giedke, L. M. K. Vandersypen, M. D. Lukin, and J. I. Cirac, Universal Quantum Transducers Based on Surface Acoustic Waves, *Phys. Rev. X* **5**, 031031 (2015).
- [15] A. Bienfait, K. J. Satzinger, Y. P. Zhong, H.-S. Chang, M.-H. Chou, C. R. Conner, E. Dumur, J. Grebel, G. A. Peairs, R. G. Povey, and A. N. Cleland, Phonon-mediated quantum state transfer and remote qubit entanglement, *Science* **364**, 368 (2019).
- [16] D. A. Golter, T. Oo, M. Amezcua, I. Lekavicius, K. A. Stewart, and H. Wang, Coupling a surface acoustic wave to an electron spin in diamond via a dark state, *Phys. Rev. X* **6**, 041060 (2016).
- [17] S. Hermelin, S. Takada, M. Yamamoto, S. Tarucha, A. D. Wieck, L. Saminadayar, C. Bäuerle, and T. Meunier, Electrons surfing on a sound wave as a platform for quantum optics with flying electrons, *Nature* **477**, 435 (2011).
- [18] R. P. G. McNeil, M. Kataoka, C. J. B. Ford, C. H. W. Barnes, D. Anderson, G. A. C. Jones, I. Farrer, and D. A. Ritchie, On-demand single-electron transfer between distant quantum dots, *Nature* **477**, 439 (2011).
- [19] M. C. Kuzyk and H. Wang, Scaling phononic quantum networks of solid-state spins with closed mechanical subsystems, *Phys. Rev. X* **8**, 041027 (2018).
- [20] Y. Chu and S. Gröblacher, A perspective on hybrid quantum opto- and electromechanical systems, *Appl. Phys. Lett.* **117**, 150503 (2020).
- [21] M. V. Gustafsson, P. V. Santos, G. Johansson, and P. Delsing, Local probing of propagating acoustic waves in a gigahertz echo chamber, *Nature Phys.* **8**, 338 (2012).
- [22] M. V. Gustafsson, T. Aref, A. F. Kockum, M. K. Ekström, G. Johansson, and P. Delsing, Propagating phonons coupled to an artificial atom, *Science* **346**, 207 (2014).
- [23] R. N. Patel, Z. Wang, W. Jiang, C. J. Sarabalis, J. T. Hill, and A. H. Safavi-Naeini, Single-mode phononic wire, *Phys. Rev. Lett.* **121**, 040501 (2018).
- [24] K. Fang, M. H. Matheny, X. Luan, and O. Painter, Optical transduction and routing of microwave phonons in cavity-optomechanical circuits, *Nature Photon.* **10**, 489 (2016).
- [25] P. Farrera, G. Heinze, and H. De Riedmatten, Entanglement between a Photonic Time-Bin Qubit and a Collective Atomic Spin Excitation, *Phys. Rev. Lett.* **120**, 100501 (2018).
- [26] J. Chan, A. H. Safavi-Naeini, J. T. Hill, S. Meenehan, and O. Painter, Optimized optomechanical crystal cavity with acoustic radiation shield, *App. Phys. Lett.* **101**, 081115 (2012).
- [27] S. Hong, R. Riedinger, I. Marinković, A. Wallucks, S. G. Hofer, R. A. Norte, M. Aspelmeyer, and S. Gröblacher, Hanbury Brown and Twiss interferometry of single phonons from an optomechanical resonator, *Science* **358**, 203 (2017).
- [28] L. Qiu, I. Shomroni, P. Seidler, and T. J. Kippenberg, Laser cooling of a nanomechanical oscillator to its zero-point energy, *Phys. Rev. Lett.* **124**, 173601 (2020).
- [29] R. Riedinger, S. Hong, R. A. Norte, J. A. Slater, J. Shang, A. G. Krause, V. Anant, M. Aspelmeyer, and S. Gröblacher, Non-classical correlations between single photons and phonons from a mechanical oscillator, *Nature* **530**, 313 (2016).
- [30] S. Weis, R. Rivière, S. Deléglise, E. Gavartin, O. Arcizet, A. Schliesser, and T. J. Kippenberg, Optomechanically Induced Transparency, *Science* **330**, 1520 (2010).
- [31] X.-L. Pang, A.-L. Yang, J.-P. Dou, H. Li, C.-N. Zhang, E. Poem, D. J. Saunders, H. Tang, J. Nunn, I. A. Walmsley, and X.-M. Jin, A hybrid quantum memory-enabled network at room temperature, *Sci. Adv.* **6**, eaax1425 (2020).
- [32] S. Gröblacher, J. T. Hill, A. H. Safavi-Naeini, J. Chan, and O. Painter, Highly efficient coupling from an optical fiber to a nanoscale silicon optomechanical cavity, *Appl. Phys. Lett.*, **103**, 181104 (2013).

SUPPLEMENTARY INFORMATION

Fabrication

The device is fabricated from a silicon-on-insulator chip with a device layer of 250 nm. We first pattern the structure using electron-beam lithography into the resist (CSAR) and then transfer it to the silicon layer with a SF_6/O_2 reactive-ion etch. The structure is then cleaned with a piranha solution and suspended by undercutting the sacrificial oxide layer using hydrofluoric acid (HF). A last cleaning step with piranha and diluted HF (1%) is performed just before mounting the sample in the dilution refrigerator.

Experimental setup

A complete overview of the experimental setup is shown in Fig. S1. The optical control pulses are created from two separate tunable CW external-cavity diode lasers. They are stabilized over time using a wavelength meter (not shown) and are filtered with fiber based filter cavities (50 MHz linewidth) to suppress the classical laser noise at GHz frequencies. We create the pulses using two 110 MHz acousto-optic modulators (AOMs) gated via a pulse generator. The optical paths are combined through a fiber beamsplitter. The pulses are routed to the device in the dilution refrigerator via an optical circulator, and then to the device's optical waveguide using a lensed fiber. The optical signal coming from the device is filtered with three 150 MHz broad free-space Fabry-Pérot cavities in series, that results into an equivalent series bandwidth of about 80 MHz. The average suppression ratio is 114 dB for the blue detuned pulse and 119 dB for the red detuned pulse (the small difference is due to small misalignment and mode mismatch of the cavities). Every ~ 10 s the experiment is paused and continuous light is sent to the filter cavities to lock them at the optical resonance of the device using optical switches. For this, the red-detuned laser is used after passing through a 50:50 beam splitter, and the detuning is compensated via an electro-optics modulator to match the optical resonance. It takes around 6 s to lock the cavities each time.

The effect of dark counts, mostly unwanted photons from stray light which couple into the fiber and leakage of pump photons through the filter chain, are negligibly small compared to the photon rate that is obtained via the Stokes and anti-Stokes scatterings. During the cross-correlation measurement shown in Fig. 3, we get total photon rates of approximately 8×10^{-4} and 1.7×10^{-4} per trial from the Stokes and anti-Stokes scatterings, respectively, from the full area of optical pulses. At the same time, the average total dark count rate, which is constant in time, is only 1×10^{-5} per trial.

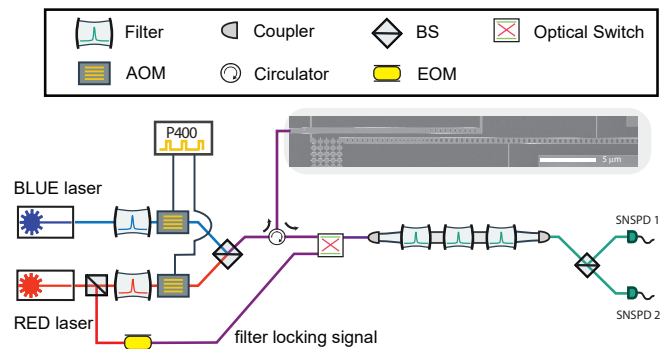


FIG. S1. The experimental setup, with BS the beam splitter and SNSPD the superconducting nanowire single-photon detectors. See text for more details.

Scattering probabilities

The Stokes and anti-Stokes scattering probabilities are determined from the click rates (Γ_r , Γ_b) on the SNSPDs and by measuring the detection efficiency of the experimental setup (η_{det})

$$\Gamma_r = p_{s,\text{read}} \cdot n_{\text{th}} \cdot \eta_{\text{det}} \quad (\text{S1})$$

$$\Gamma_b = p_{s,\text{write}} \cdot (1 + n_{\text{th}}) \cdot \eta_{\text{det}} \quad (\text{S2})$$

where the $p_{s,\text{read}}$ and $p_{s,\text{write}}$ are the scattering probabilities from the red detuned (anti-Stokes) and blue detuned (Stokes) laser pulses, respectively, and n_{th} is the mechanical mode thermal phonon occupancy. The measurement of the detection efficiency gives $\eta_{\text{det}} \approx 3.8\%$. This includes the coupling between the optical cavity and the optical coupler waveguide η_{dev} , the coupling from fiber to the optical coupler waveguide η_c , the filter setup efficiency η_F , the SNSPDs detection efficiency η_{SNSPD} , as well as all other losses in the optical path η_{loss} . Hence, the overall detection efficiency can be written as $\eta_{\text{det}} = \eta_c \cdot \eta_{\text{dev}} \cdot \eta_F \cdot \eta_{\text{SNSPD}} \cdot \eta_{\text{loss}}$. By shining a continuous off-resonance laser to the device and measuring the power at each point of the setup, we obtain $\eta_c = 37\%$, $\eta_F = 38\%$, $\eta_{\text{SNSPD}} \approx 90\%$ and $\eta_{\text{loss}} \approx 80\%$. Furthermore, the device efficiency $\eta_{\text{dev}} = \frac{\kappa_e}{\kappa_t}$ and is measured using a similar method to [32].

In the weak coupling regime ($g \ll \kappa$), the scattering probabilities are given by the efficiency ($\eta_{\text{dev}} = \frac{\kappa_e}{\kappa_t}$) and the incident laser pulse energy E_p [27]:

$$p_{s,\text{read}} = 1 - \exp\left(\frac{-4\eta_{\text{dev}}g_0^2E_p}{\hbar\omega_c(\omega_m^2 + (\kappa_t/2)^2)}\right) \quad (\text{S3})$$

$$p_{s,\text{write}} = \exp\left(\frac{4\eta_{\text{dev}}g_0^2E_p}{\hbar\omega_c(\omega_m^2 + (\kappa_t/2)^2)}\right) - 1 \quad (\text{S4})$$

where ω_c is the optical resonance frequency and ω_m the mechanical frequency.

Band structure

The band structure of the waveguide can be engineered by changing the hole dimensions and the periodicity of unit cells, while keeping the width and thickness of the beam fixed. In Fig. S2 three designs of a waveguide with different mechanical band structure and group velocity are shown. All these designs act as optical mirrors for the cavity, as can be seen from the optical band diagrams.

Lifetime

One of the fundamental properties of the device is the extremely long lifetime T_1 of the mechanical excitation. In order to measure T_1 we use a red detuned strong optical pulse to heat the device, creating a thermal population in the mode. We then send another, much weaker, red detuned pulse, to probe the thermal population as a function of time, which is directly proportional to the clickrates. The result of the measurement is shown in Fig. S3. Note that, as previously seen [7], the clickrates have a double exponential trend, with a rise time T_{rise} and a decay time T_1 . For our measurement we choose one of the shorter lifetime devices (to allow for higher repetition rates), while several structures with up to 5.5 ms are also fabricated on the same chip, as shown in the plot.

Thermal occupancy of the mechanical mode

The mechanical modes, having a frequency of around 5 GHz, have a thermal occupation of $< 10^{-5}$ at 20 mK. Due to absorption of the optical pulses used to create and read the state, the thermal occupation during the experiment is however significantly higher. We measure the mode temperature via the sideband asymmetry as shown in figure Fig. S4a. In more detail, we send a blue-detuned and red-detuned optical pulse with exactly equal energies (and thus equal scattering probabilities) and a long delay between (few times of the mechanical lifetime in order to reinitialize to the ground state at the starting of each pulse) and measure the click rates from each pulse (Γ_r, Γ_b). Using Eq. S1 and S2, we extract the thermal occupancy for different scattering probabilities. This measurement allows us calibrate the mode heating that occurs during the optical red-detuned (anti-Stokes) pulse, the instantaneous heating. To mimic the real experimental conditions with two pulses (as used for Fig. 3a), we send an additional red detuned pulse to the device 170 ns before the pulses used to measure the thermal occupation, which effectively heats the mechanical mode. The results are shown in Fig. S4b, where the x-axis is the inferred scattering probability of the heating pulse.

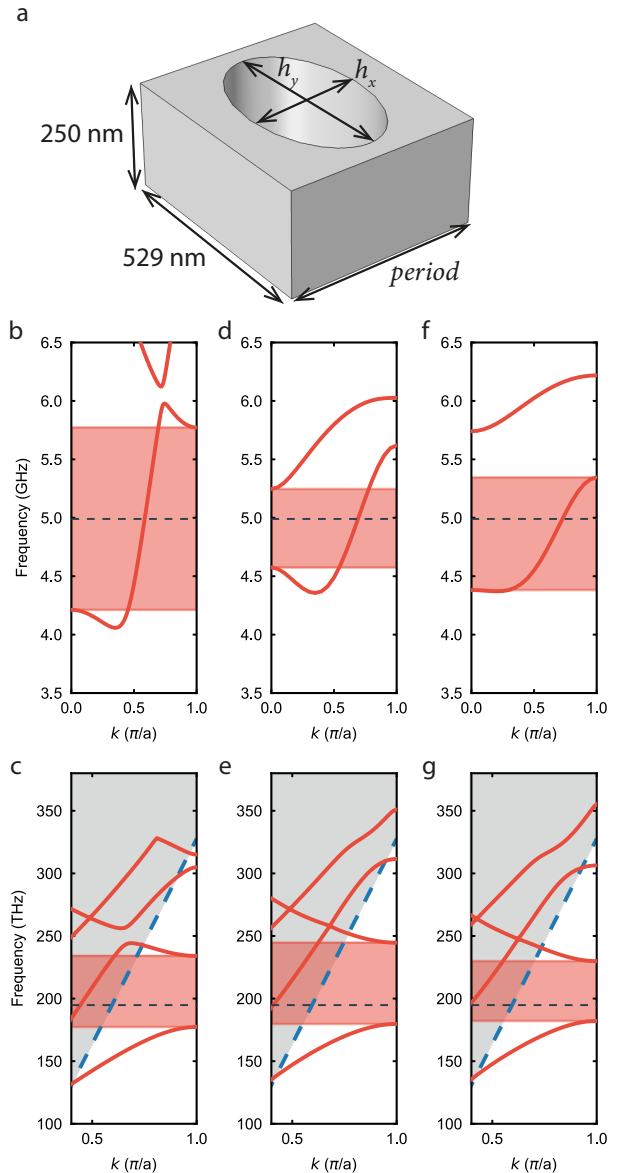


FIG. S2. Engineering the band structure and phonon group velocity by adjusting the hole dimensions: h_x diameter along the waveguide orientation, h_y , diameter perpendicular to the waveguide orientation, and the size of the unit cell (period). A sketch of the unit cell is shown in a). b,c) Mechanical and optical band diagram for a waveguide with parameters of $h_y = 187$ nm, $h_x = 320$ nm, $period = 436$ nm resulting in a mechanical group velocity of $v_g = 1946$ m/s. d,e) Parameters of $h_y = 430$ nm, $h_x = 272$ nm, $period = 458$ nm, with $v_g = 2766$ m/s. f,g) Parameters of $h_y = 468$ nm, $h_x = 240$ nm, $period = 458$ nm, with $v_g = 6298$ m/s. In our experiment, we use the second set of parameters (shown in d) and e)) in order to have a small group velocity, while simultaneously maintaining a linear region of the mechanical band to minimize dispersion.

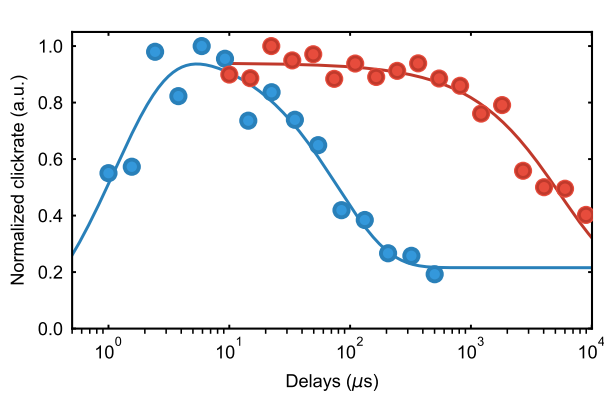


FIG. S3. Normalized clickrates (directly proportional to the thermal population) from a thermally excited mechanical mode as a function of time. The population exhibits a double exponential behavior, which corresponds to the initial heating and subsequent decay. For the device used in the measurements the rise and decay times are $T_{\text{rise}} \approx 1 \mu\text{s}$ and $T_1 \approx 78 \mu\text{s}$ (data in blue), respectively. An exemplary second device with much longer decay time $T_1 \approx 5.5 \text{ms}$ is also shown (data in red). The solid lines are exponential fits to the data.

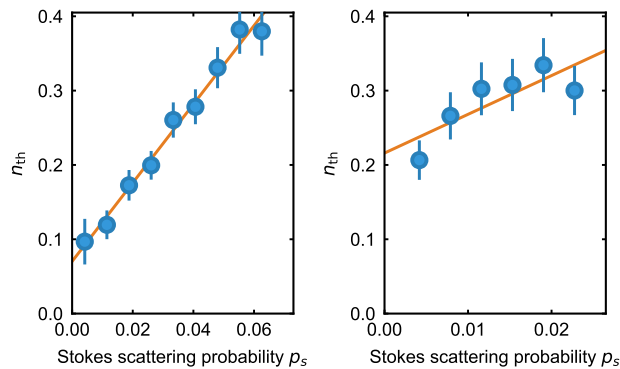


FIG. S4. a) Thermal occupation of the mode of interest as a function of the scattering probability of the Stokes and anti-Stokes process $p_{\text{s,write}} = p_{\text{s,read}} = p_{\text{s}}$. n_{th} is measured from the asymmetry of Stokes/anti-Stokes scattering rates. The fit follows $n_{\text{th}} = (0.070 \pm 0.0095) + (5.29 \pm 0.25) \times p_{\text{s}}$. We choose to work at $p_{\text{s,read}} = 1.4\%$. b) Thermal occupation with the pulse scheme of the experiment as a function of the inferred scattering probability of the anti-Stokes process for the heating pulse. Here a heating pulse is sent to the device 170 ns before the pulses used to measure the thermal occupation. Since the heating dynamics is similar for both Stokes and anti-Stokes processes, we can send either a red-detuned or a blue-detuned pulse as heating pulse. The fitting of the resulting data follows $n_{\text{th}} = (0.216 \pm 0.028) + (5.21 \pm 1.88) \times p_{\text{s}}$. Choosing a scattering probability of $p_{\text{s,write}} = 1.4\%$ results in a total thermal occupation of $n_{\text{th}} \approx 0.27$. In both figures the fits are linear and the errors are one standard deviation.

Error on the $g_{\text{om}}^{(2)}$

As discussed in the main text, we record the coincidences from the same trial ($N_{\Delta n=0}$, where n is an indicator for each experimental round), and the average number of coincidences from different trials ($\overline{N}_{\Delta n \neq 0}$), which is expected to be uncorrelated. In order to calculate the $g_{\text{om}}^{(2)}$ we divide these two quantities, such that $g_{\text{om}}^{(2)}(t) = N_{\Delta n=0}(t)/\overline{N}_{\Delta n \neq 0}(t)$. Using $\Delta n \gg 1$, one can gather enough statistics to estimate $\overline{N}_{\Delta n \neq 0}$ with a negligible error. For the estimation of the error on $N_{\Delta n=0}$, which dominates the statistical uncertainty, a binomial distribution function is considered for the number of coincidences on each trial. Therefore, from this distribution, the probability of getting different numbers of coincidences can be calculated and thus, the error of the number of coincidences will be estimated. This is similar to the method used in [29].

Double Pulse $g_{\text{om}}^{(2)}(t)$

In this experiment we use two write and two read pulses. In Fig. S5a, the click rates are shown in time. The two pairs of pulses are clearly overlapping, since the delay between them is close to their FWHM. We gather coincidences from the shaded area of the pulses, choosing them to not overlap to not double count coincidences. We use a similar technique to the one use for Fig. 3, with filtering the coincidences in a 6 ns time window with varying delays, in order to obtain finer time resolution. In Fig. S5b, the cross correlation between these fine-filtered coincidences is shown as a function of delay between them for different combinations of write and read pulse. The maximum cross correlation of these plots is depicted in Fig. 4b. Note that the maximum cross correlation for "early-early" and "late-late" combinations happen at $t \approx 170 \text{ns}$ which matches the second round trip of phonons, as expected.

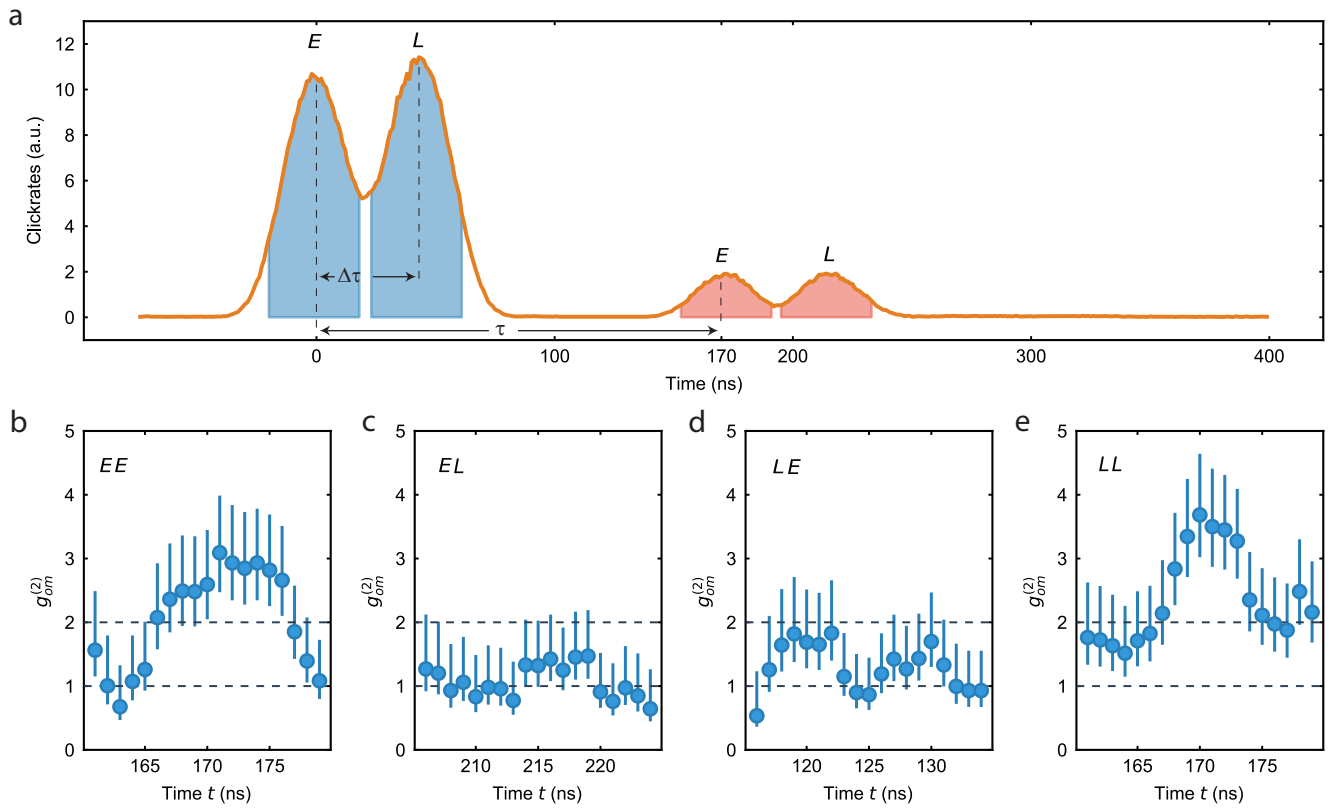


FIG. S5. a) Double-pulse click rate versus time. The two slightly overlapping write pulses preceding the read pulses are clearly distinguishable into earlier and later time. The delay between pulses is $\tau = 170$ ns for both "early-early" and "late-late" combinations, $\tau + \Delta\tau = 215$ ns for "early-late", and $\tau - \Delta\tau = 125$ ns for "late-early". b) Cross correlation between coincidences having a delay not more than 10 ns deviation from the delay between pulses, for different combinations. In all figures here "E" ("L") stands for "early" ("late").